

Moisture and Moist Static Energy Budgets of South Asian Monsoon Low Pressure Systems in GFDL AM4.0

ÁNGEL F. ADAMES^a

NOAA/Geophysical Fluid Dynamics Laboratory, Princeton, New Jersey, and University Corporation for Atmospheric Research, Boulder, Colorado

YI MING

NOAA/Geophysical Fluid Dynamics Laboratory, Princeton, New Jersey

(Manuscript received 13 October 2017, in final form 20 March 2018)


ABSTRACT

The mechanisms that lead to the propagation of anomalous moisture and moist static energy (MSE) in monsoon low and high pressure systems, collectively referred to as synoptic-scale monsoonal disturbances (SMDs), are investigated using daily output fields from GFDL's atmospheric general circulation model, version 4.0 (AM4.0). On the basis of linear regression analysis of westward-propagating rainfall anomalies of time scales shorter than 15 days, it is found that SMDs are organized into wave trains of three to four individual cyclones and anticyclones. These events amplify over the Bay of Bengal, reach a maximum amplitude over the eastern coast of India, and dissipate as they approach the Arabian Sea. The structure and propagation of the simulated SMDs resemble those documented in observations. It is found that moisture and MSE anomalies exhibit similar horizontal structures in the simulated SMDs, indicating that moisture is the leading contributor to MSE. Propagation of the moisture anomalies is governed by vertical moisture advection, while the MSE anomalies propagate because of horizontal advection of dry static energy by the anomalous winds. By combining the budgets, we interpret the propagation of the moisture anomalies in terms of lifting that is forced by horizontal dry static energy advection, that is, ascent along sloping isentropes. This process moistens the lower free troposphere, producing an environment that is more favorable to deep convection. Ascent driven by radiative heating is of primary importance to the maintenance of the moisture anomalies.

1. Introduction

The Indian summer monsoon features large spatial and temporal variations in precipitation (Chang et al. 2017). Among the transient features that grow in this region are synoptic-scale disturbances that are often referred to as monsoon low pressure systems. These systems are characterized by slow westward and northward propagation and a horizontal radius of ~ 2000 km

(Godbole 1977; Krishnamurti et al. 1975, 1976; Sikka 1977; Lau and Lau 1990). The India Meteorological Department (IMD) categorizes monsoon low pressure systems according to the strength of surface wind speed. The weakest systems are defined as lows, stronger systems with surface winds between 8.5 and 16.5 m s^{-1} are defined as monsoon depressions, and the strongest systems are referred to as cyclonic storms (Saha et al. 1981; Krishnamurthy and Ajayamohan 2010; Hunt et al. 2016). Anomalous anticyclones are also observed during the Indian monsoon, which have structures similar to the low pressure systems but with reversed polarity (Krishnamurthy and Ajayamohan 2010). This study focuses on the weaker lows, depressions, and the anomalous anticyclones, which we will collectively refer to as synoptic-scale monsoonal disturbances (SMDs; Krishnamurthy and Ajayamohan 2010; Ditchek et al. 2016).

 Denotes content that is immediately available upon publication as open access.

^a Current affiliation: Department of Climate and Space Sciences and Engineering, University of Michigan, Ann Arbor, Michigan.

Corresponding author: Ángel F. Adames, afadames@umich.edu

DOI: 10.1175/JAS-D-17-0309.1

© 2018 American Meteorological Society. For information regarding reuse of this content and general copyright information, consult the [AMS Copyright Policy](https://www.ametsoc.org/PUBSReuseLicenses) (www.ametsoc.org/PUBSReuseLicenses).

During their life cycle, monsoon low pressure systems often make landfall over the Indian subcontinent, producing up to half of the total monsoon rainfall received by India (Stano et al. 2002; Ding and Sikka 2006; Yoon and Chen 2005; Yoon and Huang 2012). Conversely, anomalous anticyclones are associated with breaks in the monsoon, with little or no rainfall occurring during the passage of these systems. Thus, understanding SMDs is of critical importance to our understanding of the Indian monsoon and its variability.

In spite of the important role that SMDs have in the monsoon's hydrologic cycle, very few studies have analyzed how these systems modulate rainfall. Many studies have assumed that SMDs are a result of a variant of baroclinic instability called moist baroclinic instability [Salvekar et al. 1986; Krishnakumar et al. 1992; Krishnamurti et al. 2013; see also Cohen and Boos (2016) for a review on the topic], with precipitation being a result of large-scale quasigeostrophic (QG) ascent in these disturbances (Shukla 1978; Mak 1983; Sanders 1984). Other studies have included moist convection in the form of frictional convergence feedbacks (Goswami 1987).

To the best of our knowledge, the first study to examine the water vapor budget of SMDs was Yoon and Chen (2005). They found that the leading balance in SMDs involves import of moisture through convergence and loss of moisture through condensation and precipitation. Their study, however, only considered the Eulerian temporal tendency in moisture over a limited domain near the center of the vortex. Thus, their study does not take into account the propagation of the moisture anomalies. However, recent studies have shown that SMDs are characterized by large specific humidity anomalies on the order of 0.3 g kg^{-1} (Krishnamurthy and Ajayamohan 2010) and lower-tropospheric relative humidity values of over 80% (Hunt et al. 2016). The large amplitude of specific humidity together with the ~ 5 -day time scale of SMDs suggests that the temporal tendency in moisture may not be negligible. Understanding the evolution of moisture may lead to novel insights into the dynamics of SMDs. Moreover, while several studies have analyzed the thermodynamic budget of SMDs (Saha and Saha 1988; Sørland and Sorteberg 2015), no study has looked at this budget in the context of moist processes, nor has any study looked at both the moisture and thermodynamic budgets within the context of moist static energy (MSE).

The goal of this study is to analyze the moisture and MSE budgets of SMDs. To carry out this analysis, we will make use of daily fields from GFDL's atmospheric general circulation model (AGCM). We use this model because it captures the main features of SMDs and because it does not exhibit the large residuals in

moisture/MSE budgets that reanalysis products have as a result of the data assimilation process (Mapes and Bacmeister 2012). Additionally, previous studies have shown that models are able to simulate SMDs reasonably well (Ashok et al. 2000; Sabre et al. 2000; Stowasser et al. 2009; Sørland et al. 2016; Hunt and Turner 2017). We will show that the propagation of the moisture anomalies is governed by vertical moisture advection while propagation of the MSE anomalies is predominantly due to horizontal MSE advection. While these two processes may seem distinct, we will show that horizontal dry static energy advection can induce vertical motion, which in turn induces a moisture tendency through vertical moisture advection. Ascent driven by radiative heating, in turn, plays a key role in maintaining the moisture anomalies.

This study is structured as follows. The next section describes GFDL's AGCM, version 4.0 (AM4.0), and the methods of analysis. Section 3 describes the Indian monsoon mean state and variability as simulated by AM4.0. Sections 4 and 5 discuss the moisture and MSE budgets of SMDs, respectively. Section 6 synthesizes the results from the two budgets. A concluding discussion is offered in section 7.

2. Data and methods

a. Model description

Most of the analysis presented here is made using daily output data from AM4.0 (Zhao et al. 2018a,b). AM4.0 uses a finite-volume, cubed-sphere topology with ~ 100 -km resolution per cube face. The output resolution used here is on a $1.25^\circ \times 1^\circ$ longitude–latitude grid. The model contains 33 vertical hybrid sigma–pressure levels (Simmons and Burridge 1981) extending from the surface to 1 hPa. Convection is parameterized in terms of a double plume scheme, which is similar to the shallow convection scheme described in Bretherton et al. (2004a) but extended to include an additional plume to represent deep convection. Further details about the model configuration and its initial performance have been documented by Zhao et al. (2018a,b).

The simulations presented here are made using prescribed present-day sea surface temperature boundary conditions (Zhao et al. 2018a). The experiments are run for 1 year as spinup and then run for an additional 10 years. We analyze the last 10 years of the simulation. Because we are mainly interested in the dynamics of SMDs in this model, we restrict our analysis to the boreal summer months of June–September (JJAS).

The following AM4.0 fields are used in this study: the horizontal winds u and v , geopotential height Z , specific

humidity q , precipitation P , dry static energy s , frozen moist static energy h , surface and top of the atmosphere shortwave (SW) and longwave (LW) radiative fluxes, and surface sensible H and latent heat fluxes E . In addition to daily data from AM4.0, two other datasets are used in this study. We make use of the $1.5^\circ \times 1.5^\circ$ horizontal resolution, daily geopotential height and wind data from ERA-Interim (Dee et al. 2011) for the 33-yr time period of 1979–2011. Rainfall data from the Tropical Rainfall Measuring Mission product 3B42 (TRMM-3B42; Huffman et al. 2007) from 1998 to 2011 are also used in this study.

b. Methods

Many of the results shown in the following sections are obtained through linear regression analysis, following the method described in Adames and Wallace (2014). We create a time series that describes the evolution of SMDs over the Bay of Bengal. Daily precipitation data, filtered to retain time scales shorter than 15 days and westward-propagating zonal wavenumbers 3–25 using the method of Hayashi (1979), are used to create this index. We chose this time scale and these zonal wavenumbers so that it fully captures the spectral signal associated with these disturbances, as will be shown in the next section. While we have verified that our results are reproducible using a 10- or 20-day high-pass filter, it is possible that our regression maps also contain a signal in the 10–20-day time scale of intraseasonal variability in this region (Annamalai and Slingo 2001).

The filtered data were averaged over the longitude–latitude box of $85^\circ\text{--}90^\circ\text{E}$, $15^\circ\text{--}20^\circ\text{N}$, where SMD activity is strongest (Sikka 1977; Godbole 1977; Boos et al. 2015). This method is similar to the method employed by Yoon and Chen (2005) and Chen et al. (2005). The index is standardized, and the anomaly patterns correspond to a one-standard-deviation anomaly of the precipitation time series. The statistical significance of the regression patterns was tested via a two-tailed t test, and the contour and shading intervals are selected to roughly represent the 95% confidence interval.

In section 3, we make use of space–time spectral analysis, following the methods of Wheeler and Kiladis (1999) and Hendon and Wheeler (2008). To extract the signal of SMDs, the time series of precipitation is divided into 60-day segments that overlap by 30 days. The segments are tapered to zero through the use of a Hanning window. We also use a Hanning window in longitude to emphasize tropical wave activity occurring over the longitude range of $50^\circ\text{--}130^\circ\text{E}$. After tapering, complex fast Fourier transforms (FFTs) are computed in longitude and then in time. Finally, the power spectrum is averaged over all segments and over

the $10^\circ\text{--}25^\circ\text{N}$ latitude belt. The number of degrees of freedom is calculated to be ~ 40 [2 (amplitude and phase) $\times 10$ (years) $\times 122$ (days in JJAS)/60 (segment length)]. We calculate the signal as $(P_{xx} - P_{\text{red}})/P_{xx}$, where P_{red} is the red spectrum, calculated using Eq. (1) of Masunaga (2007), and a value of 0.3 is considered to be statistically significant in this study. We have found the analysis to be insensitive to the length of the spatial Hanning window or the choice of segment length as long as the SMD activity is captured by the spectral analysis.

In sections 4–6, the vertically integrated moisture and frozen MSE budgets of SMDs are presented. The vertically integrated moisture is defined as

$$\langle q \rangle = \frac{1}{g} \int_{p_t}^{p_s} q dp, \quad (1)$$

where $g = 9.8 \text{ m s}^{-2}$ is the gravitational acceleration, $p_t = 100 \text{ hPa}$, and $p_s = 1000 \text{ hPa}$. All field variables in angle brackets are vertically integrated this way. Some of these budget terms exhibit large residuals because of numerical errors in the calculations of the budgets. These errors arise from the complex topography characteristic of South Asia, from the calculation of numerical gradients and from the interpolation from the model's native grid to the coordinate system used here. To reduce these residuals, we apply the adjustment method described in the appendix of Hill et al. (2017). This method adds a barotropic adjustment to the horizontal wind field in order to satisfy conservation of column-integrated moisture/MSE. Using this method largely reduces the residual from these numerical errors.

Additionally, in sections 4–6, we employ a compositing technique in space that smooths out small-scale noise in the moisture and MSE budget terms so that the synoptic-scale structure of the SMD-related processes can be brought out more clearly. We will refer to this technique as an SMD composite. In this procedure, we generate multiple maps by shifting the longitude–latitude box of the SMD index ($85^\circ\text{--}90^\circ\text{E}$, $15^\circ\text{--}20^\circ\text{N}$) by up to 2° north or south and/or west or east. For example, regression maps are generated by using indices centered on $85^\circ\text{--}90^\circ\text{E}$, $14^\circ\text{--}19^\circ\text{N}$ or $85^\circ\text{--}90^\circ\text{E}$, $16^\circ\text{--}21^\circ\text{N}$. Each of these maps is then shifted such that the center of the moisture/MSE anomalies is centered over the $85^\circ\text{--}90^\circ\text{E}$, $15^\circ\text{--}20^\circ\text{N}$ box. The SMD composite is then obtained by averaging all of the regression maps.

3. Monsoonal mean state and variability in AM4.0

Figure 1 shows the JJAS-mean 850-hPa geopotential height and horizontal winds for AM4.0 and ERA-Interim. AM4.0 captures the main features of the

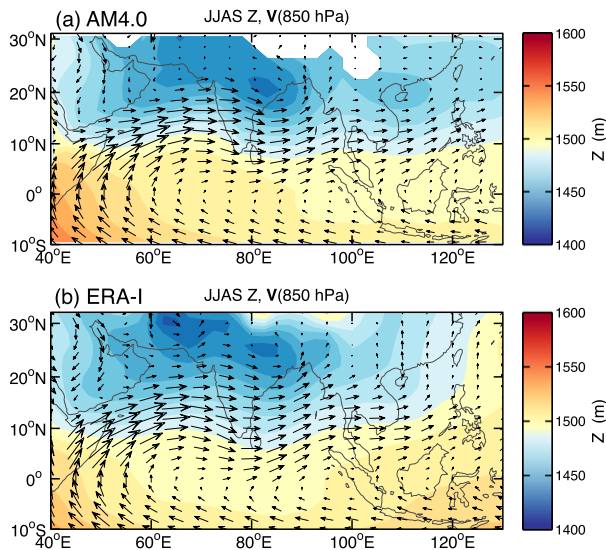


FIG. 1. Mean JJAS 850-hPa geopotential height (shading) and horizontal flow (arrows) for (a) AM4.0 and (b) ERA-Interim. The longest arrows correspond to winds of $\sim 15 \text{ m s}^{-1}$. White areas in (a) correspond to regions where the Z field is beneath the surface.

monsoonal circulation. The simulated monsoon trough is situated over northeast India, with the corresponding increase in height southward toward the Indian Ocean. A low-level westerly jet is seen in the area where the height gradient is strongest. There are also some differences with respect to ERA-Interim. AM4.0 exhibits stronger westerlies that extend farther eastward past the Philippines, and the geopotential height gradient is stronger. The difference in the westerly jet is further shown in Fig. 2, along with moisture, precipitation, and its variability. Mean precipitation (Figs. 2a,b) in AM4.0, while of similar magnitude to TRMM, occurs at different locations with respect to observations. TRMM shows rainfall maxima along the western coast of India and over the northeastern Bay of Bengal. AM4.0 exhibits a broader region of rainfall over northwest India that extends eastward and merges with a second region of maximum rainfall that is centered over the Bay of Bengal. The standard deviation of JJAS precipitation, shown in Fig. 2b, exhibits similar spatial patterns. Additionally, it is clear that TRMM precipitation exhibits a larger variance than the model does. This may be related to the inability of coarse-resolution GCMs to fully represent the topographic features of South Asia, thus not adequately representing their effects on precipitation.

Column-integrated water vapor, shown in Fig. 2c, exhibits horizontal pattern in AM4.0 that is consistent with reanalysis, although AM4.0 slightly overestimates column water in comparison to ERA-Interim. Column dry static energy, shown in Fig. 2d, exhibits slightly

smaller values in AM4.0 than ERA-Interim. Nonetheless, the two datasets exhibit similar horizontal patterns, revealing that dry static energy (DSE) increases with latitude during JJAS over southern Asia. It will be shown in subsequent sections that this positive meridional DSE gradient plays a central role in the propagation of the SMDs. Column MSE, shown in Fig. 2e, is similar to column moisture except the MSE maximum is shifted northward.

Figure 3a shows the JJAS signal strength of precipitation in AM4.0 averaged over the 10° – 25° N latitude belt. Variability in the South Asian monsoon region is governed by westward-propagating synoptic-scale disturbances (zonal wavenumbers 3–25) with time scales between 3 and 15 days. This range of zonal and temporal scales is consistent with the documented scale of SMDs (Sikka 1977; Godbole 1977; Stano et al. 2002; Hunt et al. 2016). A weaker signal is also seen at eastward-propagating zonal wavenumbers 1–20 and time scales longer than 30 days, likely in association with the boreal summer intraseasonal oscillation (BSISO). In comparison, the signal strength for TRMM-3B42 rainfall, shown in Fig. 3b, is slightly weaker but shows a nearly identical signal, with peak strength also occurring near zonal wavenumber 10 and 5-day time scales.

Based on the space–time variability in Fig. 3, we construct an SMD index by filtering daily precipitation in order to retain westward-propagating zonal wavenumbers 3–25 and time scales of 15 days and shorter (dashed box in Fig. 3). We have verified that our results are robust to different choices of the filter as long as the frequencies and wavenumbers where SMD activity is strongest are included (see Fig. 3). The filtered precipitation field is then averaged over the 85° – 90° E, 15° – 20° N box. Regression maps of the horizontal structure of SMDs is shown in Fig. 4. At lag day -2 , an anticyclonic feature is seen over northeast India, with negative precipitation anomalies centered near and to the west of the maximum height anomalies. This anticyclone reaches a peak amplitude over India and dissipates as it reaches the Arabian Sea at lag day 1. The anomalous anticyclone is followed by a cyclonic anomaly coupled to enhanced precipitation. The region of enhanced rainfall is first seen developing near the coast of Myanmar at lag day -2 . At lag day -1 , the precipitation anomalies have amplified and propagated west toward the Bay of Bengal. These anomalies are centered between the minimum height anomalies and anomalous northerly flow, consistent with observations (Warner 1984; Chen et al. 2005; Hunt et al. 2016) and previous modeling studies (Ashok et al. 2000; Sabre et al. 2000; Stowasser et al. 2009; Hunt and Turner 2017). In subsequent days, the region of enhanced precipitation follows a pattern similar to the

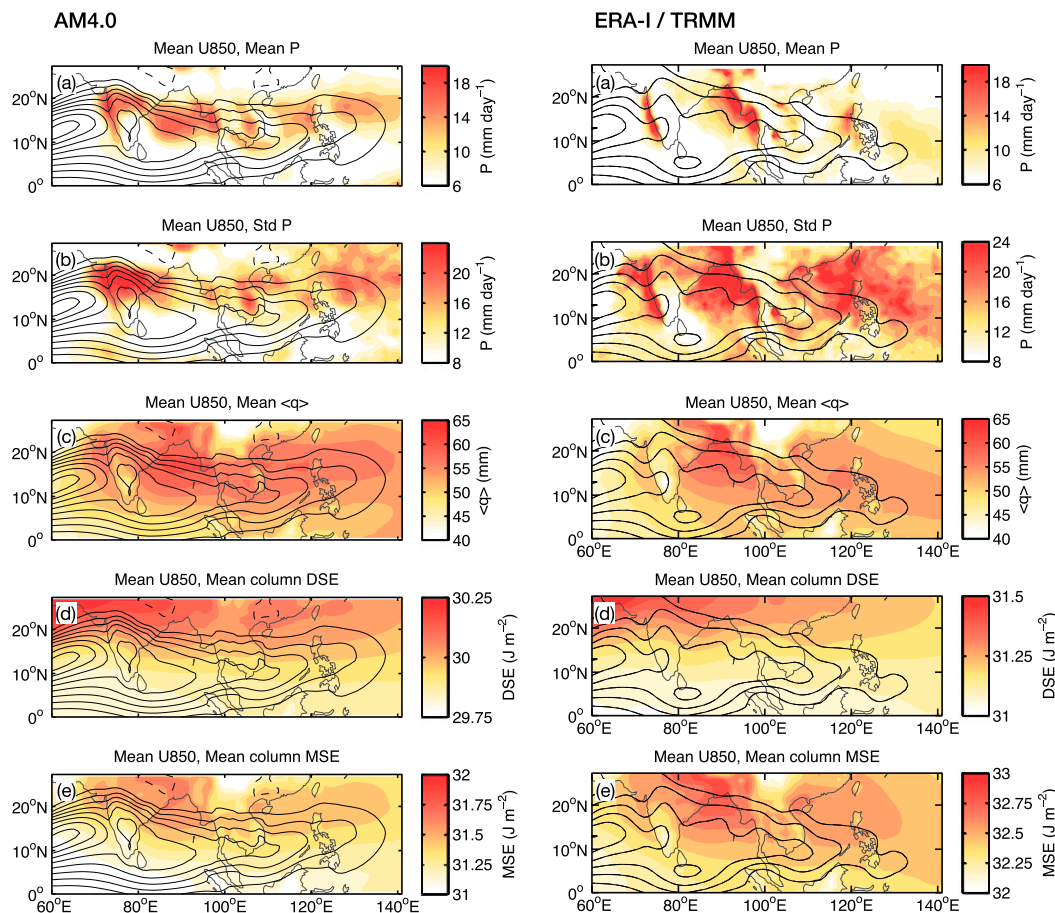


FIG. 2. Mean JJAS 850-hPa zonal wind (contours) and (a) mean JJAS precipitation, (b) standard deviation of JJAS precipitation, (c) JJAS column-integrated water vapor $\langle q \rangle$, (d) column DSE, and (e) column MSE for (left) AM4.0 and (right) ERA-Interim and TRMM-3B42 precipitation. The contour interval is 2.5 m s^{-1} ; (d) and (e) are scaled by a factor of 10^8 .

anticyclone that preceded it. The horizontal structure and propagation of the depressions in Fig. 4 are similar to those seen in Fig. 2 of Daggupaty and Sikka (1977) and Fig. 4 of Yoon and Chen (2005).

We can obtain some insights into the vertical structure of the simulated SMDs by analyzing longitude–height cross sections. Figure 5 shows a cross section of anomalous geopotential height Z' , meridional winds v' , vertical velocity ω' , and specific humidity q' overlaid by the meridionally averaged zonal mass circulation ($\rho u'$, $\rho w'$). We see that Z' and v' are largely confined to the lower troposphere and exhibit a maximum amplitude near the surface, with little signature in the upper troposphere. Ascent is a maximum in the midtroposphere over the Bay of Bengal, exhibiting a structure reminiscent of a first baroclinic mode in vertical motion. Descent to the west is a maximum at ~ 250 hPa, exhibiting a more top-heavy structure. Figure 5 (middle) shows that q' is largely

confined to the lowest levels of the troposphere, exhibiting a maximum between 850 and 900 hPa near 88°E and a minimum 650 hPa and $\sim 75^\circ\text{E}$. Both q' and, to a lesser degree, v' and Z' exhibit westward tilt with height above the 700-hPa layer and eastward tilt with height beneath it. Although not as pronounced, such tilting is also seen in the observational study of Krishnamurthy and Ajayamohan (2010). We speculate that this tilt may be a result of the low-level monsoon jet, which peaks near 800 hPa, advecting the anomalies more strongly in the lower free troposphere.

An interesting feature about the cross sections in Figs. 5a and 5b is the phasing between the fields. Both ω' and q' are shifted west of the region of low pressure, with ω' exhibiting a larger shift than q' . To further elucidate this phasing, Fig. 5c shows precipitation, column water vapor, and vertical velocity averaged over the same latitudinal belt. Column water vapor and precipitation

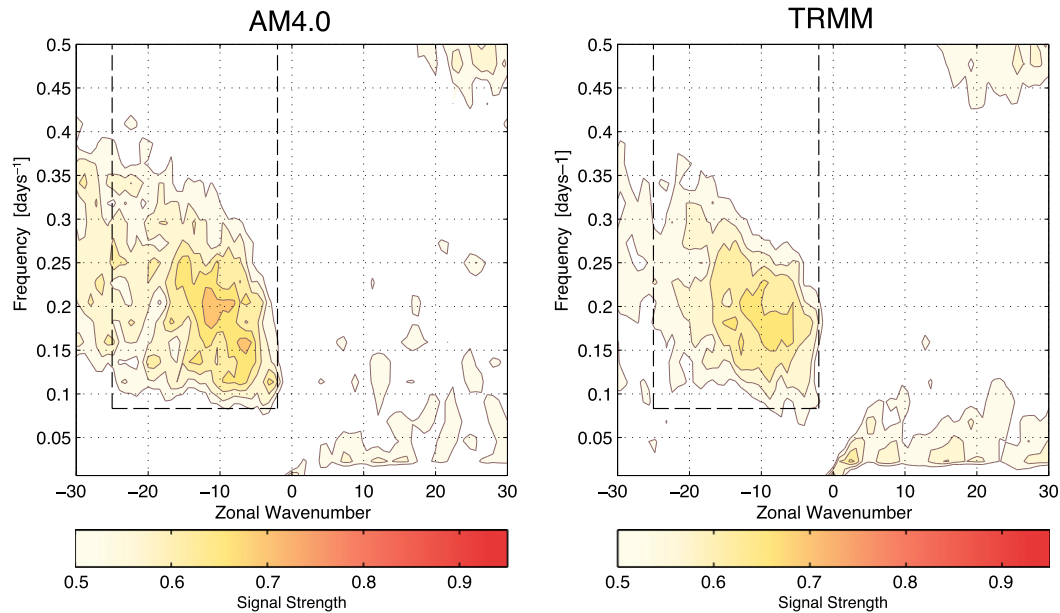


FIG. 3. Signal strength of (left) AM4.0 and (right) TRMM-3B42 precipitation. The signal was obtained from data around the 10°–25°N latitude belt and longitudinally tapered to emphasize the Asian monsoon region over 50°–130°E. The dashed lines highlight the box used to define the filter used to analyze SMDs in this study.

exhibit an in-phase relationship, while column-averaged ascent leads both fields by $\sim 5^\circ$ of longitude. All three fields are, in turn, shifted to the west of the minimum in Z' .

Figure 6 shows a time–longitude diagram of anomalous precipitation associated with SMDs. It is clear from this diagram that the SMDs are arranged into a packet of three to four westward-propagating vortices. Each anomaly propagates westward with a phase speed of $\sim 4 \text{ m s}^{-1}$. The maximum amplitude of the enhanced and/or suppressed anomalies progressively shifts eastward, indicating that the wave train might be characterized by an eastward group velocity.

4. Column-integrated moisture budget

In the previous section, we analyzed the mean state and variability in the South Asian monsoon as simulated by AM4.0. Precipitation variability in this region is found to be predominantly due to synoptic-scale features that resemble SMDs. In this section, we will seek to understand the evolution of the precipitation anomalies in these systems by analyzing the evolution of column-integrated moisture. Figure 7a shows column-integrated moisture and precipitation in an SMD composite. The two fields are spatially correlated, with enhanced precipitation located in regions of enhanced moisture and vice versa for regions of suppressed precipitation. The correlation is clearer in Fig. 8, which shows the two fields

in a scatterplot. A robust correlation of 0.84 is observed, further suggesting a strong coupling between the two fields. We can thus relate P' and $\langle q' \rangle$ through the linear equation $P' = \langle q' \rangle / \tau_c$, where τ_c is a convective moisture adjustment time scale (Bretherton et al. 2004b). Through linear least squares fit, we find that the two fields are related by a time scale of $\sim 4.5 \text{ h}$.

Based on the strong correlation between column moisture and precipitation in the simulated SMDs, we invoke the anomalous column-integrated moisture budget to understand the temporal evolution of moisture and the impact of moist processes in the anomalous precipitation region:

$$\frac{\partial \langle q' \rangle}{\partial t} = -\langle \mathbf{V} \cdot \nabla q' \rangle - \left\langle \omega \frac{\partial q}{\partial p} \right\rangle' + E' - P', \quad (2)$$

where \mathbf{V} is the horizontal wind field, ω is the pressure velocity, and E' is the anomalous surface evaporation. Primed angle brackets correspond to the same vertical integral defined in section 2, but for 15-day high-pass-filtered fields.

The contribution of each term in Eq. (2) to the propagation of the moisture anomalies is shown in Figs. 7 and 9. Precipitation (Fig. 7a) and vertical moisture advection (Fig. 7b) are the leading-order terms and largely cancel one another. The sum of the two terms (Fig. 9b) is $\sim 15\%$ as large as the individual terms that compose it. It moistens the atmosphere in regions of

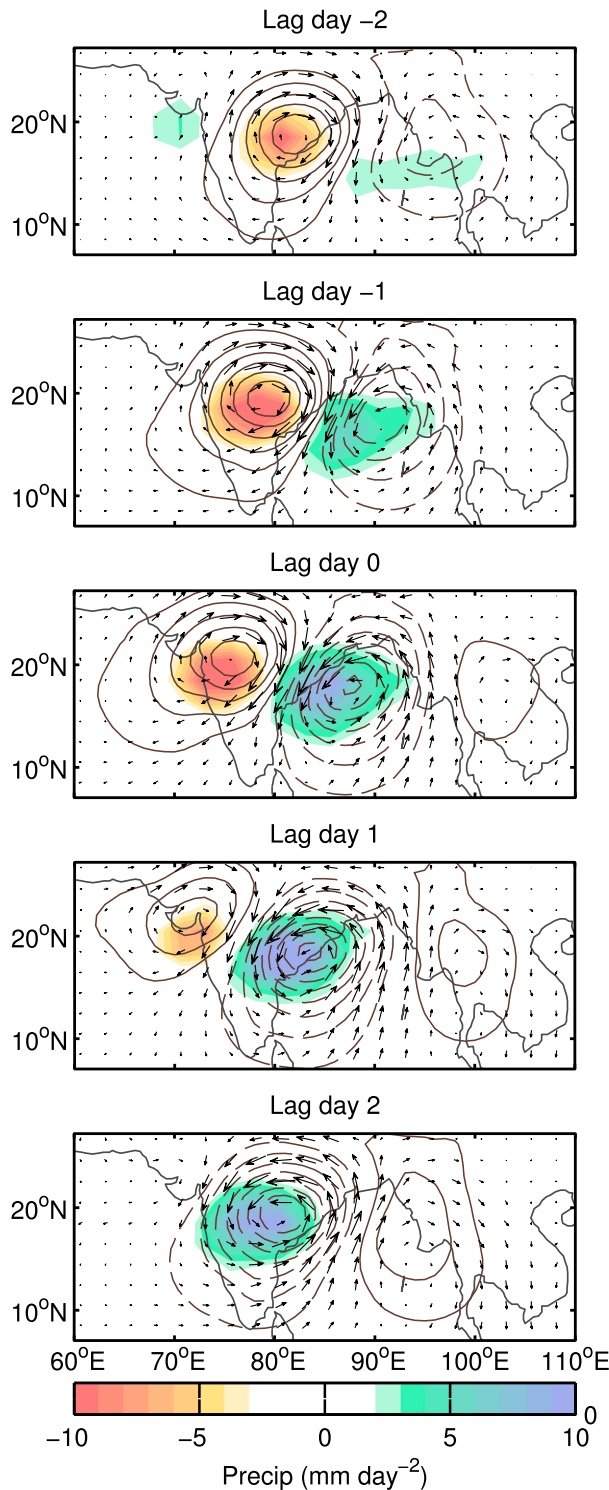


FIG. 4. Five-panel sequence of AM4.0 anomalous precipitation (shading), 850-hPa Z' (contoured), and the anomalous horizontal winds (arrows) regressed onto precipitation data filtered to retain time scales shorter than 15 days and westward-propagating zonal wavenumbers 3–25, averaged over 85°–90°E, 15°–20°N (top to bottom) Lag regression are at days –2, –1, 0, 1, and 2. The contour interval is 1.5 m. The longest arrows correspond to wind anomalies of $\sim 2 \text{ m s}^{-1}$.

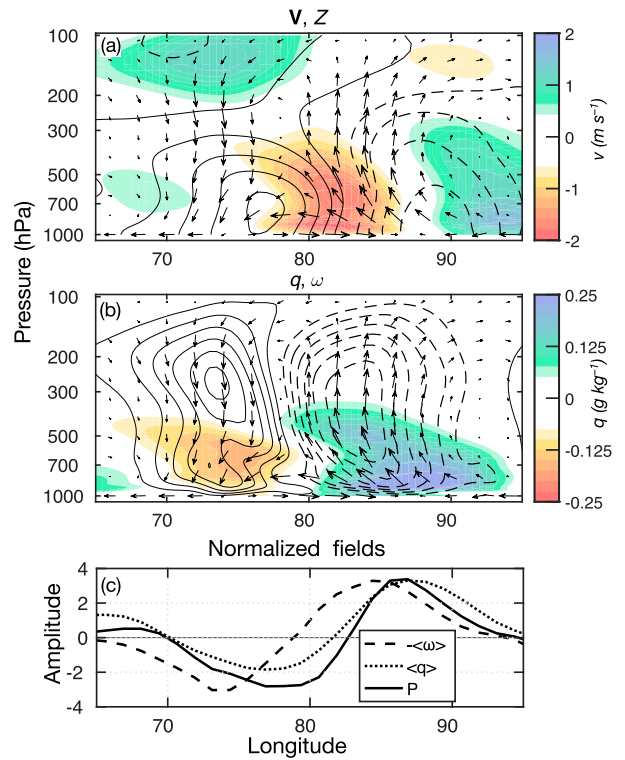


FIG. 5. Longitude–height cross section of a monsoon low pressure system at lag day 0 averaged over the 10°–25°N latitude belt. (a) Meridional wind (shading) and geopotential height (contours) anomalies. Contour interval is 1.5 m. (b) Specific humidity q (shading) and vertical velocity (contours). Contour interval is 5 hPa day^{–1}. The zonal mass circulation averaged over the 10°–25°N latitude belt is shown as arrows in (a) and (b). The largest zonal flux vector is about $0.5 \text{ kg m}^{-2} \text{ s}^{-1}$, and the largest vertical flux vector is about $0.001 \text{ kg m}^{-2} \text{ s}^{-1}$. (c) Anomalous column-averaged vertical velocity, precipitation, and column water vapor averaged over the 10°–25°N latitude belt. The fields have been normalized by their standard deviation to facilitate comparison.

anomalous northerly flow and dries in regions of southerly flow. We see that $\langle \omega \partial q / \partial p \rangle - P'$ is largely in phase with the moisture tendency in Fig. 9a, although they do not exhibit the poleward tilt with longitude that the column moisture tendency shows (Fig. 9a). This result indicates that ascent, which was shown to be shifted westward of $\langle q' \rangle$ in Fig. 5, moistens the atmosphere prior to the maximum in anomalous precipitation. The sum of all the budget terms yields a negligibly small residual (not shown).

In comparison, horizontal moisture advection is largely in phase with the moisture anomalies and acts to damp them, with an additional component that shifts the moisture tendency poleward. Surface evaporation anomalies, shown in Fig. 9d, contribute little to the propagation of the moisture anomalies, only exhibiting significant anomalies over the Bay of Bengal.

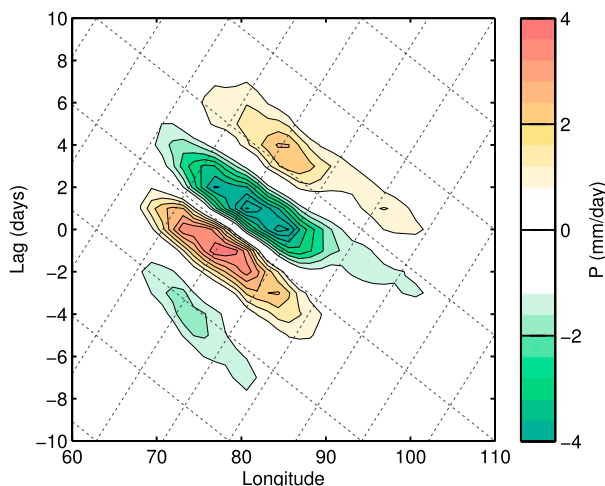


FIG. 6. Time-longitude diagram of anomalous precipitation obtained from a lag regression of the SMD index described in section 2. The fields have been averaged over the 10° – 25° N latitude belt. The contour interval is 0.2 mm day^{-1} . The dotted lines that slant westward with increasing time represent constant phase speeds of -4 m s^{-1} . The lines that slant eastward correspond to phase speeds of 2 m s^{-1} .

We can assess the relative importance of the terms in Eq. (2) to the maintenance and propagation of $\langle q' \rangle$ by comparing their projections upon the $\langle q' \rangle$ and its tendency, following the methods of Andersen and Kuang (2012), Arnold et al. (2013), and Adames et al. (2016):

$$S_m(F) = \frac{\|F\langle q' \rangle\|}{\|\langle q' \rangle\langle q' \rangle\|}, \quad (3a)$$

$$S_p(F) = \frac{\|F\partial\langle q' \rangle/\partial t\|}{\|(\partial\langle q' \rangle/\partial t)(\partial\langle q' \rangle/\partial t)\|}, \quad (3b)$$

where F corresponds to the right-hand-side terms in Eq. (2). The contribution of each term to the propagation and maintenance of the moisture anomalies is shown in Fig. 10. It is clear that the propagation of the moisture anomalies is governed by $\langle \omega \partial q / \partial p \rangle - P'$, with little contribution from horizontal moisture advection and surface evaporation. Vertical moisture advection imports moisture into the low pressure system, maintaining the region of anomalous precipitation against dissipation from horizontal moisture advection.

Our results are qualitatively consistent with the analysis of Yoon and Chen (2005), who looked at the moisture budget of SMDs in ERA-40. They also found that the leading terms are vertical moisture advection (moisture convergence in their framework) and precipitation. However, they found that the total moisture

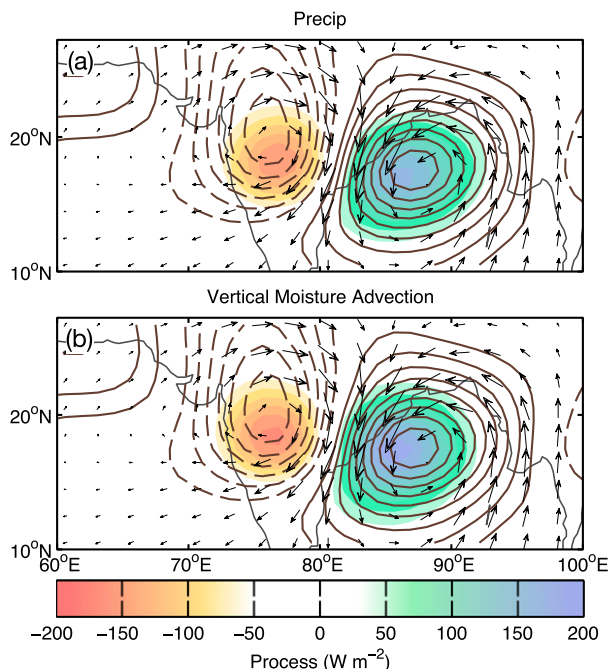


FIG. 7. SMD composite at lag day 0 of anomalous column-integrated water vapor (contours) and (a) anomalous precipitation (shading) and (b) column-integrated vertical moisture advection (shading). The contour interval is $0.25 \times 10^6 \text{ J m}^{-2}$. The SMD composite is constructed by generating multiple regression maps from SMD indices that are slightly shifted in space (see section 2b). Each of these maps is then shifted such that the center of the moisture/MSE anomalies is centered over the 85° – 90° E, 15° – 20° N box. The SMD composite is an average of all the regression maps. The terms are multiplied by $L_v = 2.5 \times 10^6 \text{ J kg}^{-1}$ to facilitate comparison with the MSE budget. The 850-hPa anomalous horizontal winds are shown as arrows in (a) and (b). The longest arrows correspond to wind anomalies of $\sim 2 \text{ m s}^{-1}$.

tendency in SMDs was small. This may be largely explained by the small $10^{\circ} \times 10^{\circ}$ box centered on the center of the vortex. Comparing with Fig. 9, it is clear that the use of this box tends to cancel out the positive moisture tendency to the west of the region of maximum anomalous precipitation and negative moisture tendency to the east. Yoon and Chen (2005) also found that surface evaporation anomalies play a larger role in SMDs than what is found here.

5. Frozen moist static energy budget

In the previous section, we analyzed the column-integrated moisture budget in order to understand the propagation of the precipitation anomalies in SMDs. It was shown that the difference between vertical moisture advection and precipitation explain the majority of the moisture tendency in SMDs. Because these two terms have a larger amplitude than the other terms in the

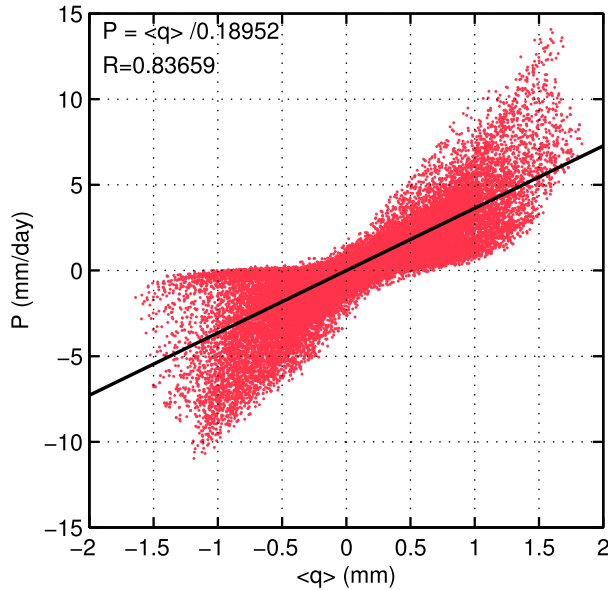


FIG. 8. Scatterplot of anomalous column-integrated water vapor $\langle q' \rangle$ and precipitation P from all points within the 60° – 100° E, 10° – 25° N domain in the regression maps that make up the SMD composite. The linear least squares fit line is shown (thick black). The slope of the linear fit (days) is shown in the top left, along with the linear correlation coefficient.

moisture budget, it may be more useful to analyze the frozen moist static energy (FMSE) budget, which we will refer to as MSE. MSE has the advantage that it is approximately conserved with the inclusion of latent heat release and thus may provide further insights onto the leading moistening processes found in the previous section. We define the frozen moist static energy h as in Bretherton et al. (2005) and Andersen and Kuang (2012):

$$h = C_p T + gZ + L_v q - L_s q_i, \quad (4)$$

where T is temperature, q_i is the ice mixing ratio, L_v is the latent energy of vaporization, L_s is the latent energy of sublimation, and C_p is the specific heat of dry air at constant pressure. The sign convention in Eq. (4) is due to the warming of the atmosphere caused by condensation and the cooling effect of sublimation. The MSE budget takes the following form:

$$\frac{\partial \langle h' \rangle}{\partial t} \simeq -\langle \mathbf{V} \cdot \nabla h \rangle' - \left\langle \omega \frac{\partial h}{\partial p} \right\rangle' + \langle LW' \rangle + \langle SW' \rangle + H' + L_v E', \quad (5)$$

where $\langle LW' \rangle$ and $\langle SW' \rangle$ are the longwave and shortwave column radiative heating anomalies, respectively, and H' is the surface sensible heat flux. Note that the left-hand side can be more accurately described by the sum

of internal energy and potential energy, taking into account the phase changes of water vapor (Hill et al. 2017). Nonetheless, h is commonly used as an approximation, and our results are unaffected by this definition.

The column frozen MSE anomalies along with their tendency are shown in Fig. 9e. The $\langle h \rangle$ anomalies are broadly similar to the $\langle q \rangle$ anomalies shown in the left column, indicating that most of the $\langle h \rangle$ anomalies are attributed to the contribution from moisture. The plot of $\partial \langle h' \rangle / \partial t$ also exhibits a similar horizontal pattern to $\partial \langle q' \rangle / \partial t$.

The leading terms in the $\langle h' \rangle$ budget are shown in the right column of Fig. 9. The largest contribution to the propagation of $\langle h' \rangle$ is horizontal MSE advection. This pattern differs significantly than that of horizontal moisture advection in Fig. 9b, indicating that advection of DSE explains the observed advection. This is consistent with previous studies of observed SMDs, who found significant warm-air advection (equivalent to positive horizontal DSE advection) to the west of the center of low pressure in SMDs (Krishnamurti et al. 1976; Saha and Chang 1983; Saha and Saha 1988; Sørland and Sorteberg 2015). Horizontal MSE advection nearly matches the pattern of $\partial \langle h' \rangle / \partial t$ and is similar to the spatial pattern of the column moisture process. Vertical MSE advection acts to offset horizontal MSE advection, but it is also shifted slightly eastward, acting to damp the MSE anomalies. Anomalous longwave radiative heating, while exhibiting smaller amplitude, is largely in phase with the MSE anomalies.

The results shown in Fig. 9 indicate that horizontal DSE advection is key to the propagation of the MSE anomalies. To further elucidate the physical processes that induce horizontal MSE advection, we separate it into contributions arising from interactions from different temporal scales, following the methods of Maloney (2009), Kiranmayi and Maloney (2011), and Adames et al. (2016):

$$-\langle \mathbf{V} \cdot \nabla h \rangle' \simeq -\langle \mathbf{V}' \cdot \nabla \bar{h} \rangle' - \langle \bar{\mathbf{V}} \cdot \nabla h' \rangle' - \langle \mathbf{V}' \cdot \nabla h' \rangle', \quad (6)$$

where overbars denote 15-day low-pass-filtered data. The terms on the right-hand side of Eq. (6) correspond to horizontal advection of low-frequency MSE by the high-frequency winds, horizontal advection of high-frequency MSE by the low-frequency winds, and the nonlinear advection of anomalous MSE by the anomalous winds. The contribution of each term to horizontal MSE advection is shown in Fig. 11. It is clear that horizontal advection of low-frequency MSE by the high-frequency winds is the leading-order term and explains most of the MSE tendency. The other two terms are small and only contribute to shift the MSE tendency

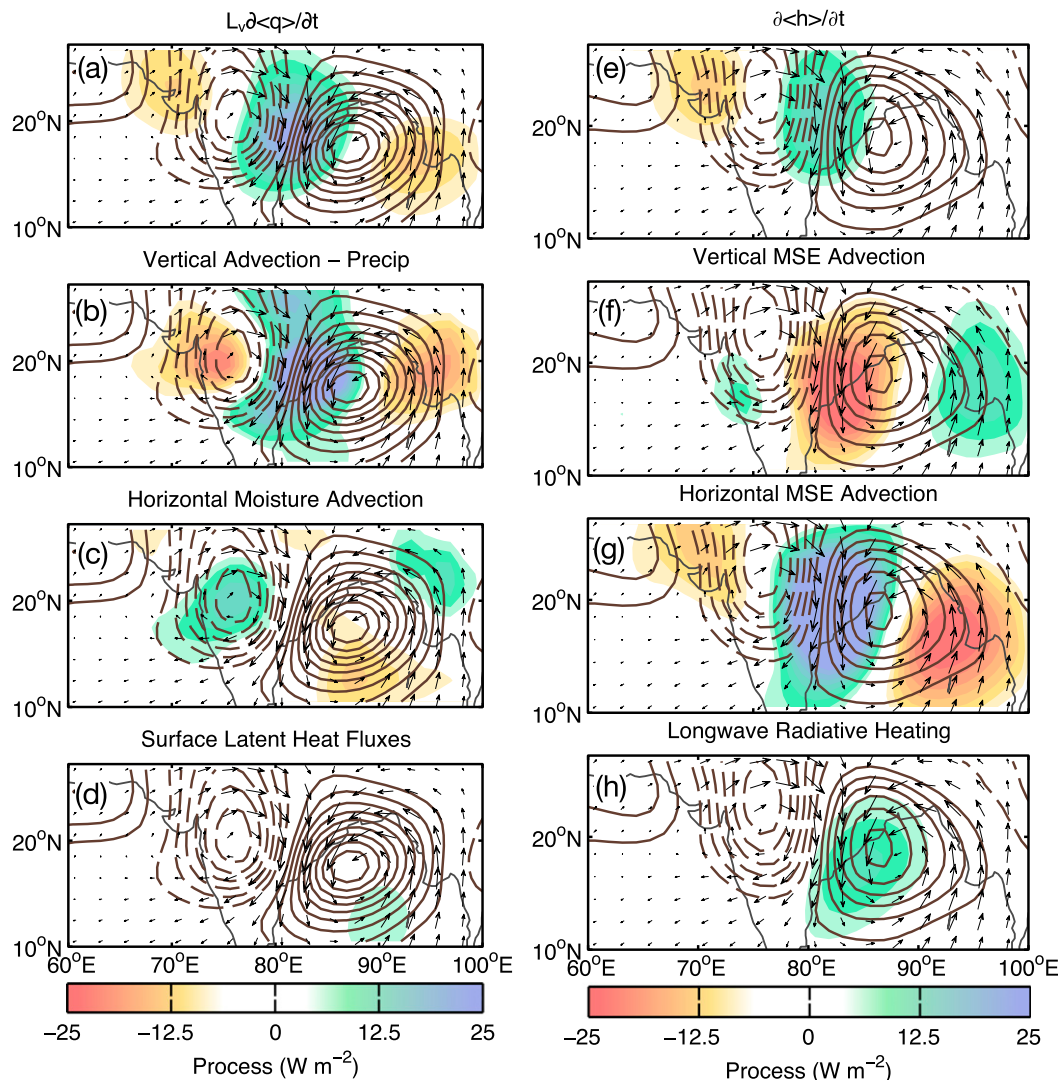


FIG. 9. SMD composite at lag day 0 of the (a)–(d) column-integrated moisture and (e)–(h) MSE budgets. In (a)–(d) column moisture is the contoured field, and (a) moisture tendency, (b) sum of vertical moisture advection and precipitation, (c) horizontal moisture advection, and (d) surface latent heat fluxes are the shaded fields. In (e)–(h) column MSE is the contoured field, and (e) the column MSE tendency, (f) vertical MSE advection, (g) horizontal MSE advection, and (h) longwave radiative heating are the shaded fields. Shading is in units of W m^{-2} . The contour interval is $0.25 \times 10^6 \text{ J m}^{-2}$. The 850-hPa anomalous horizontal winds are shown as arrows. The longest arrows correspond to wind anomalies of $\sim 2 \text{ m s}^{-1}$.

northward. The sum of the three terms approximately captures the total horizontal MSE advection shown in Fig. 9g. Since horizontal MSE advection is predominantly due to DSE advection, it implies that advection of the mean DSE in Fig. 2d by the anomalous winds is the largest contributor to horizontal MSE advection.

The contribution of each term to the propagation and maintenance of MSE is shown in Fig. 10b. It is clear that horizontal MSE advection is the largest contributor to the propagation of the MSE anomalies, with

some offset from vertical MSE advection. Longwave radiative heating maintains MSE against vertical MSE advection.

6. Bridging the budgets

In sections 4 and 5, we analyzed the column moisture and moist static energy budgets, respectively, to understand the propagation of anomalous moisture in SMDs. We found that the difference between vertical moisture advection and precipitation explains the propagation of

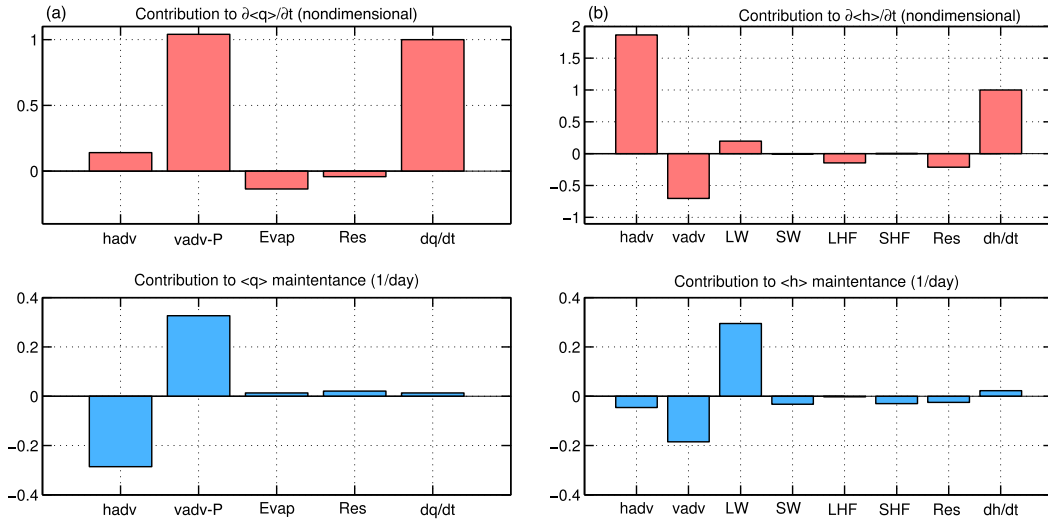


FIG. 10. Normalized contribution of the individual terms in the (a) column-integrated moisture and (b) MSE budgets to the (top) maintenance and (bottom) propagation of the regressed SMDs. The terms are obtained by projecting (top) $\langle q' \rangle$ and $\langle h' \rangle$ and (bottom) $\partial \langle q' \rangle / \partial t$ and $\partial \langle h' \rangle / \partial t$ onto the individual contributions to the moisture/MSE budget using Eq. (3). The terms of the moisture budget are, from left to right, horizontal moisture advection, the sum of vertical moisture advection and precipitation, surface evaporation, the residual after adding all terms, and the moisture tendency. The MSE budget terms are, from left to right, horizontal MSE advection, vertical MSE advection, longwave radiative heating, shortwave radiative heating, surface latent heat fluxes, surface sensible heat fluxes, the residual, and the MSE tendency.

the moisture anomalies, while horizontal DSE advection is the leading-order process in the propagation of the MSE anomalies. In this section, we will show how these two processes are physically related. The leading thermodynamic balance can be written in terms of a dry static energy budget with little loss of accuracy, as described by Sobel et al. (2014):

$$\left(\omega \frac{\partial s}{\partial p} \right)' \simeq -(\mathbf{V} \cdot \nabla s)' + Q'_c + Q'_r - \frac{\partial s'}{\partial t}, \quad (7)$$

where Q'_c and Q'_r are the convective and radiative contributions to apparent heating. Following the method of Chikira (2014), Wolding et al. (2016), and Adames (2017), we can separate the pressure velocity term into four contributions, one from horizontal DSE advection ω_a , one from radiative heating ω_r , one from convective heating ω_c , and one from the DSE tendency ω_s . If we assume that perturbations in the vertical DSE gradient are much smaller than those of the background DSE gradient, we can obtain the following:

$$\omega'_a \simeq -(\partial \bar{s} / \partial p)^{-1} (\mathbf{V} \cdot \nabla s)', \quad (8a)$$

$$\omega'_c \simeq (\partial \bar{s} / \partial p)^{-1} Q'_c, \quad (8b)$$

$$\omega'_r \simeq (\partial \bar{s} / \partial p)^{-1} Q'_r, \quad (8c)$$

$$\omega'_s \simeq -(\partial \bar{s} / \partial p)^{-1} \partial s' / \partial t, \quad (8d)$$

where the overbar refers to time scales longer than 15 days. Note that ω'_a is an adiabatic term, while ω'_c and ω'_r are diabatic; ω'_s can be thought as a residual term that accounts for the DSE tendency.

By combining Eqs. (2) and (8), it becomes clear that different processes contribute to vertical motion: convective and radiative heating, horizontal DSE advection, and the DSE tendency. The ω'_a , in particular, is related to ascent that occurs as air parcels move along sloping isentropic surfaces (isentropic ascent). The contribution of each process to total vertical motion is shown in Fig. 12. Ascent in association with convective heating is the leading-order term and predominantly contributes to the maintenance of the moisture anomalies. Ascent in association with positive DSE advection is smaller in magnitude and is responsible for shifting the vertical velocity anomalies west of the region of maximum precipitation, as seen in Fig. 5. Radiative heating and the DSE tendency contribute less to the total vertical motion and are approximately in phase with the convective heating. A residual exists that is of a similar magnitude as the radiative and DSE tendency terms (dotted lines), likely due to errors in the analysis and vertical motion related to nonlinear interactions.

We can further investigate the contributions of the aforementioned components of vertical motion to the moisture advection. Figure 13a shows that

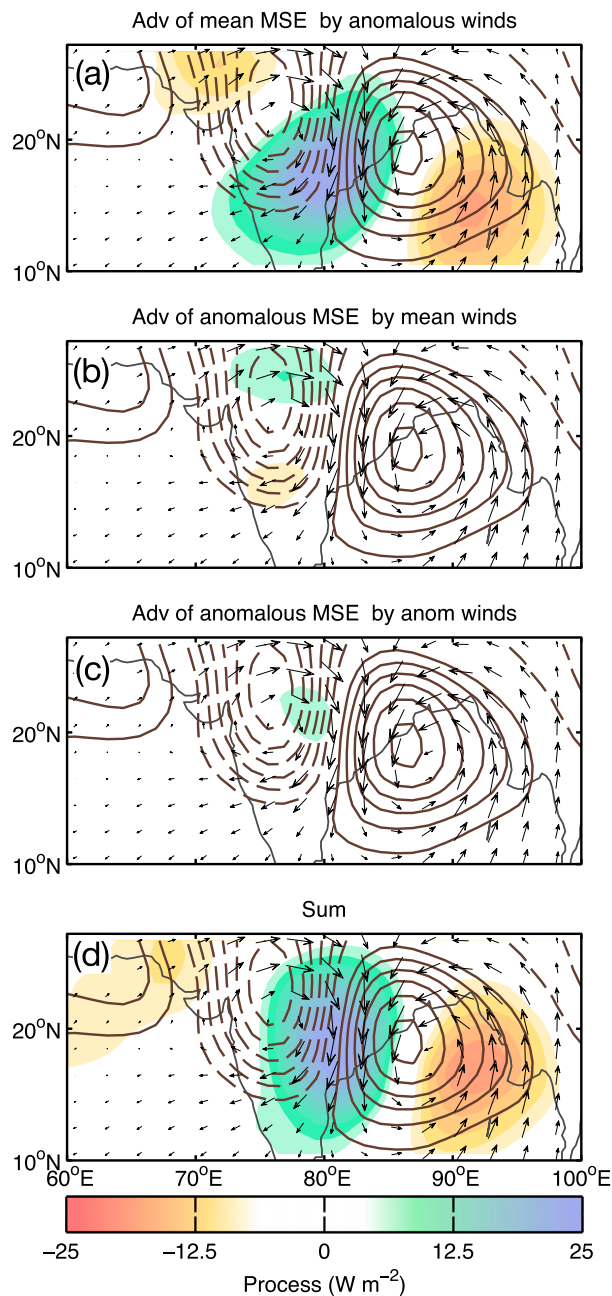


FIG. 11. As in Fig. 9, but the shaded fields show (a) horizontal advection of low-frequency MSE by the high-frequency winds, (b) horizontal advection of high-frequency MSE by the low-frequency winds, (c) horizontal advection of high-frequency MSE advection by the high-frequency winds, and (d) the sum of (a)–(c). The 850-hPa anomalous horizontal winds are shown as arrows. The longest arrows correspond to wind anomalies of $\sim 2 \text{ m s}^{-1}$.

vertical moisture advection from ω'_a is largely in phase with $\partial\langle q' \rangle / \partial t$, with a spatial correlation of ~ 0.9 over the $60^\circ\text{--}100^\circ\text{E}$, $10^\circ\text{--}25^\circ\text{N}$ domain (not shown). The contributions from ω'_r are approximately in phase with the

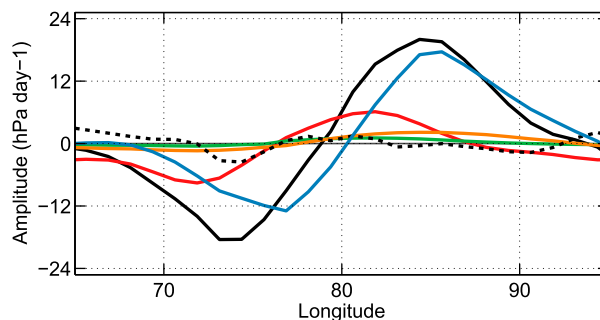


FIG. 12. (a) As in Fig. 5c, but showing column-averaged $-\omega$ as a black solid line, $-\omega'_a$ in red, ω'_c in blue, ω'_r in orange, ω'_s in green, and the residual $\omega' - \omega'_a - \omega'_c - \omega'_r - \omega'_s$ as a dotted line.

precipitation anomalies, as shown in Fig. 13b. The difference between vertical moisture advection from convectively driven ascent ω_c and precipitation is also shown in Fig. 13b. The anomalies are negative and slightly shifted to the west of P' , suggesting that it damps the moisture anomalies as well as slows its propagation. Thus, convection alone cannot explain the horizontal patterns seen in Fig. 9b. These results are summarized in Fig. 14. It is clear that isentropic ascent predominantly drives the propagation of the moisture anomalies, while ascent in association with radiative heating is the most important contributor to the maintenance of the moisture anomalies. The four terms considered here explain most of the vertical moisture advection, and the resulting residual is small.

Thus, that horizontal DSE advection contributes the most to the propagation of the MSE anomalies is consistent with the propagation of the moisture anomalies being predominantly due to the residual between the sum of vertical moisture advection and precipitation. Similarly, anomalous radiative heating induces vertical motion that supplies additional moisture to the region of anomalous precipitation in SMDs, acting to maintain it ($\omega_r \partial q / \partial p$). Thus, that radiative heating maintains the MSE anomalies is consistent with $\langle \omega \partial q / \partial p \rangle - P'$ being the leading process in the maintenance of the moisture anomalies in Fig. 10a. Both processes increase the supply of moisture to the column, thus contributing to the positive values of $\langle \omega \partial q / \partial p \rangle - P'$ seen in Fig. 9b.

7. Concluding discussion

In this study we analyzed the column moisture and MSE budgets of synoptic-scale monsoon disturbances (SMDs) as simulated by GFDL's AM4.0. AM4.0 captures a mean JJAS flow and horizontal distributions of moisture, DSE, and MSE that are consistent with those of ERA-Interim. However, the model fails to

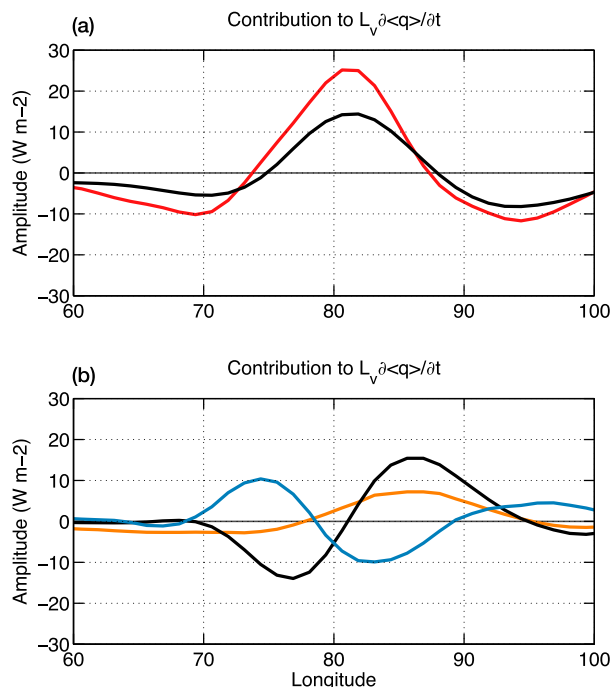


FIG. 13. SMD composite of (a) $-\langle \omega'_a \partial \bar{q} / \partial p \rangle$ (red) and $\partial \langle q' \rangle / \partial t$ (black) averaged from 10° to 25°N and (b) $-\langle \omega'_c \partial \bar{q} / \partial p \rangle - P'$ (blue), $\langle \omega'_s \partial \bar{q} / \partial p \rangle$ (orange), and P' (black) averaged from 10° to 25°N; P' has been divided by a factor of 4 to facilitate comparison.

accurately describe the distribution of climatological-mean precipitation. In spite of this caveat, the model captures SMDs that are consistent with observations (Daggupaty and Sikka 1977; Chen et al. 2005). This result suggests that SMDs might not be sensitive to the details of the climatological-mean distribution of precipitation. A schematic summarizing the main results of this study is shown in Fig. 15.

The simulated SMDs are found to exhibit a life cycle where they develop over the Bay of Bengal, attain a maximum amplitude as they make landfall over India, and then dissipate as they reach the Arabian Sea. While this life cycle is consistent with previous studies (Krishnamurthy and Ajayamohan 2010; Yoon and Chen 2005), it may also be due to our choice of index, which is centered near the coastline. A lag regression analysis reveals that these systems are arranged into wave trains of three to four events that propagate westward.

It is worth noting that the mean state in AM4.0 is characterized by excess precipitation over the tropical western North Pacific. This region was referred to in Fig. 10 of Zhao et al. (2018a) as the “Philippine hot spot.” This may increase the number of lows that propagate into the Bay of Bengal, contributing to the higher SMD spectral variance that AM4.0 exhibits with respect to TRMM-3B42 (see Fig. 3).

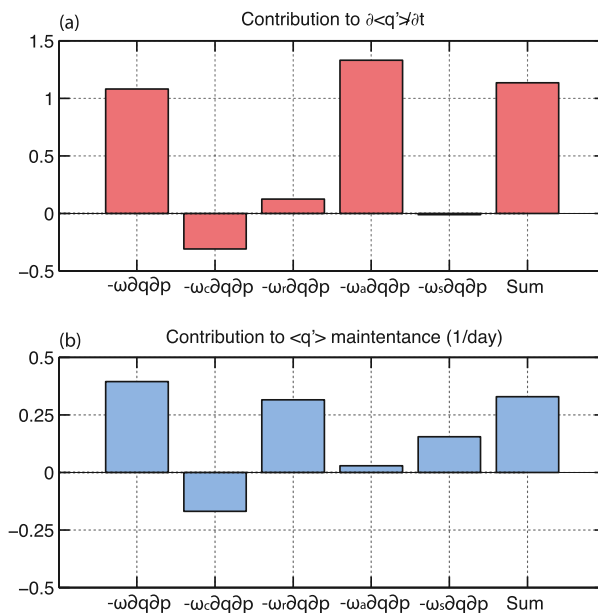


FIG. 14. (a) As in Fig. 10, but showing the contributions by, from left to right, $-\langle \omega'_a \partial \bar{q} / \partial p \rangle - P'$, $-\langle \omega'_c \partial \bar{q} / \partial p \rangle - P'$, $-\langle \omega'_i \partial \bar{q} / \partial p \rangle$, $-\langle \omega'_s \partial \bar{q} / \partial p \rangle$, $-\langle \omega'_a \partial \bar{q} / \partial p \rangle$, and the residual (difference between the first term and the next four terms) to the (a) propagation and (b) maintenance of the moisture anomalies.

The column-integrated moisture and MSE budgets of the simulated SMDs are analyzed and compared in this study. In the moisture budget, it is found that the sum of vertical moisture advection and precipitation is the largest contributor to both the propagation and maintenance of the column moisture anomalies. This moisture tendency results from anomalous vertical moisture advection slightly leading the precipitation anomalies as the SMD propagates westward, indicating that vertical moisture advection from deep ascent moistens the troposphere prior to the maximum in anomalous precipitation, as summarized in Fig. 15. Similarly, vertical moisture advection maintains the precipitation anomalies against damping by horizontal advection.

The column MSE budget reveals that the processes that maintain the moisture anomalies in SMDs differ from those that induce its propagation. Horizontal MSE advection governs the propagation of the MSE anomalies. Because the horizontal structure of MSE advection differs from that of horizontal moisture advection, it is inferred that it is predominantly due to horizontal DSE advection. When both MSE and moisture budgets are considered together, we find that horizontal DSE advection induces vertical motion. This ascent, in turn, moistens the atmosphere to the west of the maximum precipitation anomalies (red arrow in Fig. 15). Ascent

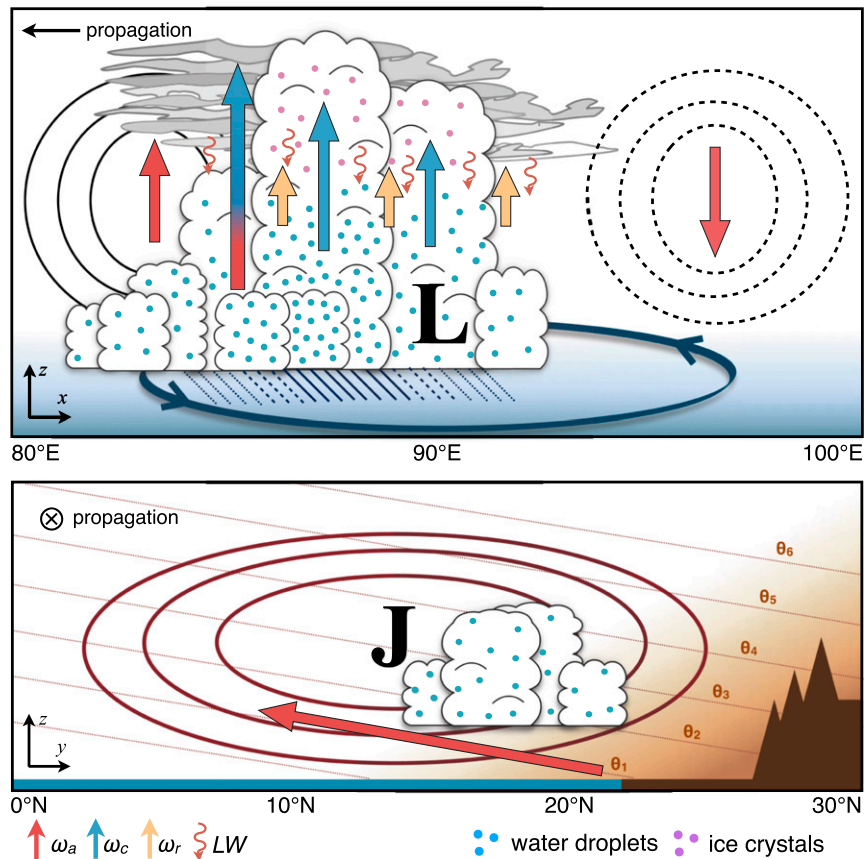


FIG. 15. Schematic describing the structure and propagation of an SMD as inferred from results of this study. (top) A longitude–height cross section and (bottom) a latitude–height cross section corresponding to the left side of the top panel ($\sim 83^\circ\text{E}$). The anomalous northerly winds (solid contours in top panel; arrow in bottom panel) advect warm air from the Indian subcontinent. This warm air ascends along lines of constant potential temperature θ (QG ascent; red vertical arrow), which moistens the free troposphere. This moistening creates a more favorable environment for deep convection (blue vertical arrows), which reaches a maximum amplitude to the west of the center of low pressure. The maximum in ascent (mixed blue and red arrow) is due to the sum of adiabatic ascent and convectively driven ascent. The rain area is maintained by the moist environment augmented by ascent driven by radiative heating (light orange arrows); L depicts the center of the low pressure system, and J represents the center of the low-level westerly jet. Flow out of the page is depicted by solid lines, and flow into the page is depicted by dashed lines. Liquid water content and ice crystals are depicted with circles, as in [Janiga and Zhang \(2016\)](#).

associated with horizontal DSE advection corresponds to lifting occurring along isentropic surfaces.

In contrast, it is found that longwave radiative heating maintains the MSE anomalies against dissipation from horizontal MSE advection. This anomalous heating induces vertical motion, which supplies the precipitation anomalies with additional water vapor (orange arrows in [Fig. 15](#)). The same mechanism is suggested to play a key role in the maintenance of the MJO ([Andersen and Kuang 2012](#); [Chikira 2014](#); [Sobel et al. 2014](#); [Wolding et al. 2016](#)) and in convective self-aggregation ([Bretherton et al. 2005](#); [Wing and Emanuel 2014](#)).

The anomalous circulations associated with radiative heating have also been shown to play a role in maintaining breaks in the Indian monsoon ([Prasanna and Annamalai 2012](#)).

Many studies have used the quasigeostrophic (QG) omega equation to diagnose the region of anomalous precipitation ([Mak 1982](#); [Sanders 1984](#)) in SMDs. In this study, QG vertical motion approximately corresponds to isentropic ascent ω'_a . Based on this traditional QG assumption, precipitation is proportional to ω'_a , and thus, both fields would be spatially in phase. However, our results indicate that ω_a is shifted west of the maximum in

anomalous precipitation by $\sim 5^\circ$. Instead of being spatially correlated with the precipitation field, QG ascent ω'_a is found to be in phase with the moisture tendency $\partial q'/\partial t$. Thus, ω_a moistens the atmosphere before precipitation increases rather than it being the cause of the precipitation. This distinction is important because it suggests that QG theory alone cannot account for the profile of vertical motion and convection in these systems. Instead, vertical motion, water vapor, and precipitation interact with the anomalous circulation. Isentropic lift acts to increase column water vapor to the west of the low pressure center, which in turn produces a thermodynamic environment that favors increased precipitation. This moist environment helps maintain the region of precipitation as it propagates west. The anomalous precipitation, in turn, is maintained by the circulation and enhanced water vapor and through interactions with radiation.

The results shown in this study contrast to those presented by Boos et al. (2015). In their analysis of the vorticity budget of monsoon depressions, they found that the nonlinear horizontal vorticity advection, or “beta drift,” is responsible for the propagation of the vortex. For the moisture and MSE budgets considered here, we found that nonlinear terms contribute little to these budgets. These differences may be attributed to the choice of index. The index used by Boos et al. (2015) is based on stronger monsoon depression, while our linear regression index may be more representative of the weaker monsoon lows. It would be interesting to repeat the analysis presented here with an index such as the one used by Boos et al. (2015).

The results presented in this study indicate that analyzing moisture and MSE budgets provide useful insights into dynamics of SMDs. It would be interesting to compare these budgets to those of easterly waves both in the Pacific and over Africa. Furthermore, incorporating these equations into a linear theoretical framework for monsoon depressions may also shed light on our understanding of these systems. Such a framework is presented in a companion paper (Adames and Ming 2018).

Acknowledgments. This work was supported by the National Oceanic and Atmospheric Administration (NOAA) Grant NA15OAR4310099. We thank Isaac Held, Kuniaki Inoue, Brian Mapes, H. Annamalai, and an anonymous reviewer for comments that have helped improve the manuscript. We would also like to thank Ming Zhao for making the AM4.0 data available to us.

REFERENCES

- Adames, Á. F., 2017: Precipitation budget of the Madden–Julian oscillation. *J. Atmos. Sci.*, **74**, 1799–1817, <https://doi.org/10.1175/JAS-D-16-0242.1>.
- , and J. M. Wallace, 2014: Three-dimensional structure and evolution of the MJO and its relation to the mean flow. *J. Atmos. Sci.*, **71**, 2007–2026, <https://doi.org/10.1175/JAS-D-13-0254.1>.
- , and Y. Ming, 2018: Interactions between water vapor and potential vorticity in synoptic-scale monsoonal disturbances: Moisture vortex instability. *J. Atmos. Sci.*, in press, <https://doi.org/10.1175/JAS-D-17-0310.1>.
- , J. M. Wallace, and J. M. Monteiro, 2016: Seasonality of the structure and propagation characteristics of the MJO. *J. Atmos. Sci.*, **73**, 3511–3526, <https://doi.org/10.1175/JAS-D-15-0232.1>.
- Andersen, J. A., and Z. Kuang, 2012: Moist static energy budget of MJO-like disturbances in the atmosphere of a zonally symmetric aquaplanet. *J. Climate*, **25**, 2782–2804, <https://doi.org/10.1175/JCLI-D-11-00168.1>.
- Annamalai, H., and J. M. Slingo, 2001: Active/break cycles: Diagnosis of the intraseasonal variability of the Asian summer monsoon. *Climate Dyn.*, **18**, 85–102, <https://doi.org/10.1007/s003820100161>.
- Arnold, N. P., Z. Kuang, and E. Tziperman, 2013: Enhanced MJO-like variability at high SST. *J. Climate*, **26**, 988–1001, <https://doi.org/10.1175/JCLI-D-12-00272.1>.
- Ashok, K., M. K. Soman, and V. Satyan, 2000: Simulation of monsoon disturbances in a GCM. *Pure Appl. Geophys. (PAGEOPH)*, **157**, 1509–1539, <https://doi.org/10.1007/PL00001131>.
- Boos, W. R., J. V. Hurley, and V. S. Murthy, 2015: Adiabatic westward drift of Indian monsoon depressions. *Quart. J. Roy. Meteor. Soc.*, **141**, 1035–1048, <https://doi.org/10.1002/qj.2454>.
- Bretherton, C. S., J. R. McCaa, and H. Grenier, 2004a: A new parameterization for shallow cumulus convection and its application to marine subtropical cloud-topped boundary layers. Part I: Description and 1D results. *Mon. Wea. Rev.*, **132**, 864–882, [https://doi.org/10.1175/1520-0493\(2004\)132<0864:ANPFC>2.0.CO;2](https://doi.org/10.1175/1520-0493(2004)132<0864:ANPFC>2.0.CO;2).
- , M. E. Peters, and L. E. Back, 2004b: Relationships between water vapor path and precipitation over the tropical oceans. *J. Climate*, **17**, 1517–1528, [https://doi.org/10.1175/1520-0442\(2004\)017<1517:RBWVPA>2.0.CO;2](https://doi.org/10.1175/1520-0442(2004)017<1517:RBWVPA>2.0.CO;2).
- , P. N. Blossey, and M. Khairoutdinov, 2005: An energy-balance analysis of deep convective self-aggregation above uniform SST. *J. Atmos. Sci.*, **62**, 4273–4292, <https://doi.org/10.1175/JAS3614.1>.
- Chang, C.-P., H.-C. Kuo, N.-C. Lau, R. H. Johnson, B. Wang, and M. C. Wheeler, Eds., 2017: *The Global Monsoon System: Research and Forecast*. 3rd ed. Asia-Pacific Weather and Climate Series, Vol. 5, World Scientific, 396 pp.
- Chen, T.-C., J.-H. Yoon, and S.-Y. Wang, 2005: Westward propagation of the Indian monsoon depression. *Tellus*, **57A**, 758–769, <https://doi.org/10.3402/tellusa.v57i5.14733>.
- Chikira, M., 2014: Eastward-propagating intraseasonal oscillation represented by Chikira–Sugiyama cumulus parameterization. Part II: Understanding moisture variation under weak temperature gradient balance. *J. Atmos. Sci.*, **71**, 615–639, <https://doi.org/10.1175/JAS-D-13-038.1>.
- Cohen, N. Y., and W. R. Boos, 2016: Perspectives on moist baroclinic instability: Implications for the growth of monsoon depressions. *J. Atmos. Sci.*, **73**, 1767–1788, <https://doi.org/10.1175/JAS-D-15-0254.1>.
- Daggupati, S. M., and D. R. Sikka, 1977: On the vorticity budget and vertical velocity distribution associated with the life cycle of a monsoon depression. *J. Atmos. Sci.*, **34**, 773–792, [https://doi.org/10.1175/1520-0469\(1977\)034<0773:OTVBAV>2.0.CO;2](https://doi.org/10.1175/1520-0469(1977)034<0773:OTVBAV>2.0.CO;2).

- Dee, D. P., and Coauthors, 2011: The ERA-Interim reanalysis: Configuration and performance of the data assimilation system. *Quart. J. Roy. Meteor. Soc.*, **137**, 553–597, <https://doi.org/10.1002/qj.828>.
- Ding, Y., and D. R. Sikka, 2006: Synoptic systems and weather. *The Asian Monsoon*, Springer, 131–201, https://doi.org/10.1007/3-540-37722-0_4.
- Ditchek, S. D., W. R. Boos, S. J. Camargo, and M. K. Tippett, 2016: A genesis index for monsoon disturbances. *J. Climate*, **29**, 5189–5203, <https://doi.org/10.1175/JCLI-D-15-0704.1>.
- Godbole, R. V., 1977: The composite structure of the monsoon depression. *Tellus*, **29**, 25–40, <https://doi.org/10.3402/tellusa.v29i1.11327>.
- Goswami, B. N., 1987: A mechanism for the west-north-west movement of monsoon depressions. *Nature*, **326**, 376–378, <https://doi.org/10.1038/326376a0>.
- Hayashi, Y., 1979: A generalized method of resolving transient disturbances into standing and traveling waves by space-time spectral analysis. *J. Atmos. Sci.*, **36**, 1017–1029, [https://doi.org/10.1175/1520-0469\(1979\)036<1017:AGMORT>2.0.CO;2](https://doi.org/10.1175/1520-0469(1979)036<1017:AGMORT>2.0.CO;2).
- Hendon, H. H., and M. C. Wheeler, 2008: Some space–time spectral analyses of tropical convection and planetary-scale waves. *J. Atmos. Sci.*, **65**, 2936–2948, <https://doi.org/10.1175/2008JAS2675.1>.
- Hill, S. A., Y. Ming, I. M. Held, and M. Zhao, 2017: A moist static energy budget-based analysis of the Sahel rainfall response to uniform oceanic warming. *J. Climate*, **30**, 5637–5660, <https://doi.org/10.1175/JCLI-D-16-0785.1>.
- Huffman, G. J., and Coauthors, 2007: The TRMM Multisatellite Precipitation Analysis (TMPA): Quasi-global, multiyear, combined-sensor precipitation estimates at fine scales. *J. Hydrometeorol.*, **8**, 38–55, <https://doi.org/10.1175/JHM560.1>.
- Hunt, K. M. R., and A. G. Turner, 2017: The effect of horizontal resolution on Indian monsoon depressions in the Met Office NWP model. *Quart. J. Roy. Meteor. Soc.*, **143**, 1756–1771, <https://doi.org/10.1002/qj.3030>.
- , —, P. M. Inness, D. E. Parker, and R. C. Levine, 2016: On the structure and dynamics of Indian monsoon depressions. *Mon. Wea. Rev.*, **144**, 3391–3416, <https://doi.org/10.1175/MWR-D-15-0138.1>.
- Janiga, M. A., and C. Zhang, 2016: MJO moisture budget during DYNAMO in a cloud-resolving model. *J. Atmos. Sci.*, **73**, 2257–2278, <https://doi.org/10.1175/JAS-D-14-0379.1>.
- Kiranmayi, L., and E. D. Maloney, 2011: Intraseasonal moist static energy budget in reanalysis data. *J. Geophys. Res.*, **116**, D21117, <https://doi.org/10.1029/2011JD016031>.
- Krishnakumar, V., R. N. Keshavamurthy, and S. V. Kasture, 1992: Moist baroclinic instability and the growth of monsoon depressions—Linear and nonlinear studies. *Proc. Indian Acad. Sci., Earth Planet. Sci.*, **101**, 123–152.
- Krishnamurthy, V., and R. S. Ajayamohan, 2010: Composite structure of monsoon low pressure systems and its relation to Indian rainfall. *J. Climate*, **23**, 4285–4305, <https://doi.org/10.1175/2010JCLI2953.1>.
- Krishnamurti, T. N., M. Kanamitsu, R. Godbole, C.-B. Chang, F. Carr, and J. H. Chow, 1975: Study of a monsoon depression (I): Synoptic structure. *J. Meteor. Soc. Japan*, **53**, 227–239, https://doi.org/10.2151/jmsj1965.53.4_227.
- , —, —, —, —, and —, 1976: Study of a monsoon depression (II): Dynamical structure. *J. Meteor. Soc. Japan*, **54**, 208–226, https://doi.org/10.2151/jmsj1965.54.4_208.
- , A. Martin, R. Krishnamurti, A. Simon, A. Thomas, and V. Kumar, 2013: Impacts of enhanced CCN on the organization of convection and recent reduced counts of monsoon depressions. *Climate Dyn.*, **41**, 117–134, <https://doi.org/10.1007/s00382-012-1638-z>.
- Lau, K.-H., and N.-C. Lau, 1990: Observed structure and propagation characteristics of tropical summertime synoptic scale disturbances. *Mon. Wea. Rev.*, **118**, 1888–1913, [https://doi.org/10.1175/1520-0493\(1990\)118<1888:OSAPCO>2.0.CO;2](https://doi.org/10.1175/1520-0493(1990)118<1888:OSAPCO>2.0.CO;2).
- Mak, M., 1982: On moist quasi-geostrophic baroclinic instability. *J. Atmos. Sci.*, **39**, 2028–2037, [https://doi.org/10.1175/1520-0469\(1982\)039<2028:OMQGBI>2.0.CO;2](https://doi.org/10.1175/1520-0469(1982)039<2028:OMQGBI>2.0.CO;2).
- , 1983: A moist baroclinic model for monsoonal mid-tropospheric cyclogenesis. *J. Atmos. Sci.*, **40**, 1154–1162, [https://doi.org/10.1175/1520-0469\(1983\)040<1154:AMBMFM>2.0.CO;2](https://doi.org/10.1175/1520-0469(1983)040<1154:AMBMFM>2.0.CO;2).
- Maloney, E. D., 2009: The moist static energy budget of a composite tropical intraseasonal oscillation in a climate model. *J. Climate*, **22**, 711–729, <https://doi.org/10.1175/2008JCLI2542.1>.
- Mapes, B. E., and J. T. Bacmeister, 2012: Diagnosis of tropical biases and the MJO from patterns in the MERRA analysis tendency fields. *J. Climate*, **25**, 6202–6214, <https://doi.org/10.1175/JCLI-D-11-00424.1>.
- Masunaga, H., 2007: Seasonality and regionality of the Madden-Julian oscillation, Kelvin wave, and equatorial Rossby wave. *J. Atmos. Sci.*, **64**, 4400–4416, <https://doi.org/10.1175/2007JAS2179.1>.
- Prasanna, V., and H. Annamalai, 2012: Moist dynamics of extended monsoon breaks over South Asia. *J. Climate*, **25**, 3810–3831, <https://doi.org/10.1175/JCLI-D-11-00459.1>.
- Sabre, M., K. Hodges, K. Laval, J. Polcher, and F. Désalmand, 2000: Simulation of monsoon disturbances in the LMD GCM. *Mon. Wea. Rev.*, **128**, 3752–3771, [https://doi.org/10.1175/1520-0493\(2001\)129<3752:SOMDIT>2.0.CO;2](https://doi.org/10.1175/1520-0493(2001)129<3752:SOMDIT>2.0.CO;2).
- Saha, K., and C.-P. Chang, 1983: The baroclinic processes of monsoon depressions. *Mon. Wea. Rev.*, **111**, 1506–1514, [https://doi.org/10.1175/1520-0493\(1983\)111<1506:TBPOMD>2.0.CO;2](https://doi.org/10.1175/1520-0493(1983)111<1506:TBPOMD>2.0.CO;2).
- , and S. Saha, 1988: Thermal budget of a monsoon depression in the Bay of Bengal during FGGE-MONEX 1979. *Mon. Wea. Rev.*, **116**, 242–255, [https://doi.org/10.1175/1520-0493\(1988\)116<0242:TBOAMD>2.0.CO;2](https://doi.org/10.1175/1520-0493(1988)116<0242:TBOAMD>2.0.CO;2).
- , F. Sanders, and J. Shukla, 1981: Westward propagating predecessors of monsoon depressions. *Mon. Wea. Rev.*, **109**, 330–343, [https://doi.org/10.1175/1520-0493\(1981\)109<0330:WPPOMD>2.0.CO;2](https://doi.org/10.1175/1520-0493(1981)109<0330:WPPOMD>2.0.CO;2).
- Salvekar, P. S., L. George, and S. K. Mishra, 1986: Low level wind shear and baroclinic growth of monsoon depression scale waves. *Meteor. Atmos. Phys.*, **35**, 10–18, <https://doi.org/10.1007/BF01029520>.
- Sanders, F., 1984: Quasi-geostrophic diagnosis of the monsoon depression of 5–8 July 1979. *J. Atmos. Sci.*, **41**, 538–552, [https://doi.org/10.1175/1520-0469\(1984\)041<0538:QGDOTM>2.0.CO;2](https://doi.org/10.1175/1520-0469(1984)041<0538:QGDOTM>2.0.CO;2).
- Shukla, J., 1978: CISK-barotropic-baroclinic instability and the growth of monsoon depressions. *J. Atmos. Sci.*, **35**, 495–508, [https://doi.org/10.1175/1520-0469\(1978\)035<0495:CBBIAT>2.0.CO;2](https://doi.org/10.1175/1520-0469(1978)035<0495:CBBIAT>2.0.CO;2).
- Sikka, D. R., 1977: Some aspects of the life history, structure and movement of monsoon depressions. *Pure Appl. Geophys. (PAGEOPH)*, **115**, 1501–1529, <https://doi.org/10.1007/BF00874421>.
- Simmons, A. J., and D. M. Burridge, 1981: An energy and angular-momentum conserving vertical finite-difference scheme and hybrid vertical coordinates. *Mon. Wea. Rev.*, **109**, 758–766, [https://doi.org/10.1175/1520-0493\(1981\)109<0758:AEAAMC>2.0.CO;2](https://doi.org/10.1175/1520-0493(1981)109<0758:AEAAMC>2.0.CO;2).
- Sobel, A., S. Wang, and D. Kim, 2014: Moist static energy budget of the MJO during DYNAMO. *J. Atmos. Sci.*, **71**, 4276–4291, <https://doi.org/10.1175/JAS-D-14-0052.1>.

- Sørland, S. L., and A. Sorteberg, 2015: The dynamic and thermodynamic structure of monsoon low-pressure systems during extreme rainfall events. *Tellus*, **67A**, 27039, <https://doi.org/10.3402/tellusa.v67.27039>.
- , —, C. Liu, and R. Rasmussen, 2016: Precipitation response of monsoon low-pressure systems to an idealized uniform temperature increase. *J. Geophys. Res. Atmos.*, **121**, 6258–6272, <https://doi.org/10.1002/2015JD024658>.
- Stano, G., T. N. Krishnamurti, T. S. V. V. Kumar, and A. Chakraborty, 2002: Hydrometeor structure of a composite monsoon depression using the TRMM radar. *Tellus*, **54A**, 370–381, <https://doi.org/10.1034/j.1600-0870.2002.01330.x>.
- Stowasser, M., H. Annamalai, and J. Hafner, 2009: Response of the South Asian summer monsoon to global warming: Mean and synoptic systems. *J. Climate*, **22**, 1014–1036, <https://doi.org/10.1175/2008JCLI2218.1>.
- Warner, C., 1984: Core structure of a Bay of Bengal monsoon depression. *Mon. Wea. Rev.*, **112**, 137–152, [https://doi.org/10.1175/1520-0493\(1984\)112<0137:CSOABO>2.0.CO;2](https://doi.org/10.1175/1520-0493(1984)112<0137:CSOABO>2.0.CO;2).
- Wheeler, M., and G. N. Kiladis, 1999: Convectively coupled equatorial waves: Analysis of clouds and temperature in the wavenumber–frequency domain. *J. Atmos. Sci.*, **56**, 374–399, [https://doi.org/10.1175/1520-0469\(1999\)056<0374:CCEWAO>2.0.CO;2](https://doi.org/10.1175/1520-0469(1999)056<0374:CCEWAO>2.0.CO;2).
- Wing, A. A., and K. A. Emanuel, 2014: Physical mechanisms controlling self-aggregation of convection in idealized numerical modeling simulations. *J. Adv. Model. Earth Syst.*, **6**, 59–74, <https://doi.org/10.1002/2013MS000269>.
- Wolding, B. O., E. D. Maloney, and M. Branson, 2016: Vertically resolved weak temperature gradient analysis of the Madden-Julian oscillation in SP-CESM. *J. Adv. Model. Earth Syst.*, **8**, 1586–1619, <https://doi.org/10.1002/2016MS000724>.
- Yoon, J.-H., and T.-C. Chen, 2005: Water vapor budget of the Indian monsoon depression. *Tellus*, **57A**, 770–782, <https://doi.org/10.3402/tellusa.v57i5.14737>.
- , and W.-R. Huang, 2012: Indian monsoon depression: Climatology and variability. *Modern Climatology*, InTech, 45–72.
- Zhao, M., and Coauthors, 2018a: The GFDL global atmosphere and land model AM4.0/LM4.0: 1. Simulation characteristics with prescribed SSTs. *J. Adv. Model. Earth Syst.*, **10**, 691–734, <https://doi.org/10.1002/2017MS001208>.
- , and Coauthors, 2018b: The GFDL global atmosphere and land model AM4.0/LM4.0: 2. Model description, sensitivity studies, and tuning strategies. *J. Adv. Model. Earth Syst.*, **10**, 735–769, <https://doi.org/10.1002/2017MS001209>.